ARL-TR-8543 • Oct 2018

US Army Research Laboratory

Transmission Electron Microscopy Characterization of Knoop Indentation Inelastic Deformation Regions in Three Commercial Silicon Carbides

by Samuel G Hirsch, Scott D Walck, Jerry C LaSalvia, and Jeffrey J Swab

NOTICES

Disclaimers

The findings in this report are not to be construed as an official Department of the Army position unless so designated by other authorized documents.

Citation of manufacturer's or trade names does not constitute an official endorsement or approval of the use thereof.

Destroy this report when it is no longer needed. Do not return it to the originator.

ARL-TR-8543 ● OCT 2018

US Army Research Laboratory

Transmission Electron Microscopy Characterization of Knoop Indentation Inelastic Deformation Regions in Three Commercial Silicon Carbides

by Samuel G Hirsch, Jerry C LaSalvia, and Jeffrey J Swab
Weapons and Materials Research Directorate, ARL

Scott D Walck
SURVICE Engineering, Belcamp, MD

REPORT DOCUMENTATION PAGE

Form Approved
OMB No. 0704-0188

1. REPORT DATE *(DD-MM-YYYY)*	2. REPORT TYPE	3. DATES COVERED (From - To)
October 2018	Technical Report	March 2015–June 2017

4. TITLE AND SUBTITLE
Transmission Electron Microscopy Characterization of Knoop Indentation Inelastic Deformation Regions in Three Commercial Silicon Carbides

5a. CONTRACT NUMBER
W911QX-16-D-0014

5b. GRANT NUMBER

5c. PROGRAM ELEMENT NUMBER

6. AUTHOR(S)
Samuel G Hirsch, Scott D Walck, Jerry C LaSalvia, and Jeffrey J Swab

5d. PROJECT NUMBER

5e. TASK NUMBER

5f. WORK UNIT NUMBER

7. PERFORMING ORGANIZATION NAME(S) AND ADDRESS(ES)
US Army Research Laboratory
ATTN: RDRL-WMM-E
2800 Powder Mill Road, Adelphi, MD 20783-1138

8. PERFORMING ORGANIZATION REPORT NUMBER
ARL-TR-8543

9. SPONSORING/MONITORING AGENCY NAME(S) AND ADDRESS(ES)

10. SPONSOR/MONITOR'S ACRONYM(S)

11. SPONSOR/MONITOR'S REPORT NUMBER(S)

12. DISTRIBUTION/AVAILABILITY STATEMENT
Approved for public release; distribution is unlimited.

13. SUPPLEMENTARY NOTES
The research reported in this document was performed in connection with contract/instrument W911QX-16-D-0014 with the US Army Research Laboratory. The views and conclusions contained in this document are those of SURVICE Engineering and the US Army Research Laboratory. Citation of manufacturer's or trade names does not constitute an official endorsement or approval of the use thereof. The US Government is authorized to reproduce and distribute reprints for Government purposes notwithstanding any copyright notation hereon.

14. ABSTRACT
Understanding the deformation mechanisms in ceramic materials that govern penetration resistance is crucial for developing better ceramic materials for lightweight body and vehicle armor systems. To determine the mechanistic response of three commercially available armor-grade silicon carbide (SiC) variants to quasi-static large contact stresses, transmission electron microscopy (TEM) was used to examine cross sections of the inelastically deformed regions beneath 1-kgf Knoop indents. Due to the potential for extensive cracking around and below the indents, a multistep sample preparation technique was developed to preserve the cross sections intact. TEM specimens were made using the focused-ion beam technique. In general, TEM characterization of the inelastically deformed regions revealed stacking faults, dislocations, transgranular and intergranular microcracking and macrocracking, which varied for each commercial SiC due to variations in their processing and resultant microstructures.

15. SUBJECT TERMS
silicon carbide, SiC, transmission electron microscopy, TEM, Knoop indentation, microstructural defect characterization

16. SECURITY CLASSIFICATION OF:			17. LIMITATION OF ABSTRACT	18. NUMBER OF PAGES	19a. NAME OF RESPONSIBLE PERSON
a. REPORT	b. ABSTRACT	c. THIS PAGE	UU	41	Samuel G Hirsch
Unclassified	Unclassified	Unclassified			19b. TELEPHONE NUMBER (Include area code) 410-306-1907

Contents

List of Figures

1. Introduction and Background

Silicon carbide (SiC) is used for armor applications because of its excellent combination of low-density, high-elastic modulus, high hardness, good fracture toughness, and good chemical inertness.[1–12] Although ceramics are relatively brittle materials, many exhibit some degree of "plasticity" under compressive loading conditions.[13–16] The role of plasticity in the ballistic response of a ceramic has long been a point of discussion. Wilkins et al. were the first to identify the apparent importance of ceramic plasticity or plastic deformation mechanisms in the ballistic performance of beryllium oxide (BeO) and aluminum nitride (AlN).[17] Later, Heard and Cline demonstrated the positive effect of lateral confinement on the inelastic response of BeO, AlN, and aluminum oxide (Al_2O_3) during compressive uniaxial loading.[18] Ballistic results by Lundberg et al. appear to present further support for the importance of ceramic plasticity on ballistic performance.[19] They showed that the compressive yield strength derived from hardness measurements of several armor ceramics appeared to correlate well with soft projectile impact velocities corresponding to penetration onset. (This is also referred to as the "dwell/penetration transition velocity".) Furthermore, Lundberg et al. showed that penetration onset velocities for boron carbide, two SiCs, titanium diboride (TiB_2), and synthetic diamond (Syndie) variants, plotted as a function of their derived compressive yield strengths (σ_Y), yielded data that appeared to fall between two curves based on perfect plasticity theory.[19] These curves, one upper bound and one lower, are related to the critical pressures corresponding to hardness ($3\sigma_Y$) and yield onset ($\sim 1.1\sigma_Y$, depends on Poisson's ratio), respectively, for blunt indentation (i.e., spherical indenter).

Using a physically based model for the inelastic behavior of geological materials under compression,[20] LaSalvia et al. showed that the lower bound curve is not unique and corresponds to ceramics with low "ductility" parameters.[21] Ductility is defined as the ratio of tensile fracture strength to yield strength in shear.[20] The implication of the ductility parameter is that for ceramics with low ductility parameter values, their inelastic response is governed by brittle fracture while those with higher values exhibit more plasticity. This is in qualitative agreement with Lundberg et al. in that the lower curve represents materials with almost no ductility while the upper curve represents materials with higher ductility.[19] If the proposed analysis is correct, then a small amount of plasticity can potentially have a significant effect on the dwell/penetration transition velocity of an armor ceramic. Note that in the context here, plasticity refers to inelastic, nonlinear deformation prior to catastrophic failure.

In general, it has long been known that hardness correlates with gross ballistic performance. It has not, however, been correlated to such a degree as to be useful for predicting ballistic performance or aiding materials' development. Hardness is considered a measure of a material's resistance to deformation or penetration. Unfortunately, it is not an inherent physical property of the material since it is influenced not only by the material's response to the indentation process, but to indenter geometry, specimen size, and interface and boundary conditions. Conceptually, the hardness–load curve can be divided into three main regions: 1) a predominantly elastic region at low indentation loads, 2) a predominantly plastic region at intermediate loads, and 3) a region of extensive permanent damage (fracture) at high loads where substantial cracking is occurring and the hardness is essentially load independent (Fig. 1).

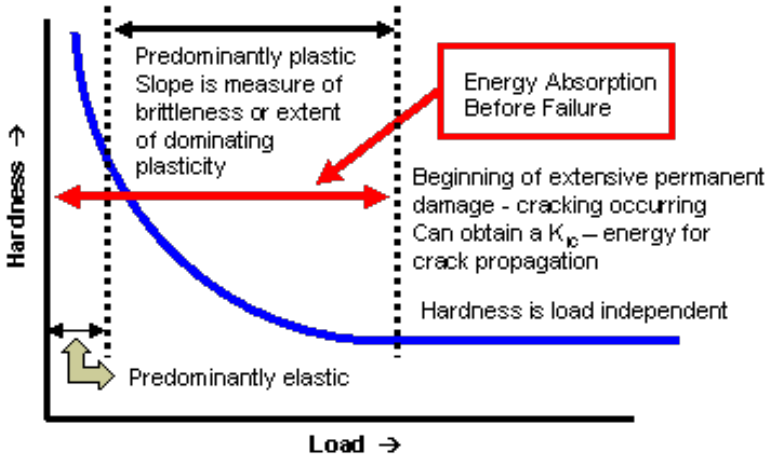

Fig. 1 Conceptualized hardness–load curve (Wilantewicz and McCauley[22])

Wilantewicz and McCauley used the exponent of a power law curve fit of the hardness–load curve as a quantitative representation of the amount of plasticity (a plasticity parameter) in structural ceramics.[22] They were able to link the plasticity parameter with a 0.98 N hardness value to predict the transitional velocity in several SiC materials. More recently, Hilton et al. refined this analysis and the associated equation leading to a robust method that predicts the transitional velocities of various SiCs to within 5% of the measured values and aluminum oxynitride (AlON) within 10%.[23]

To better understand the mechanisms of plasticity in SiC armor ceramics and the role they play in ballistic performance we have employed transmission electron microscopy (TEM) to examine thin cross sections of mechanically deformed regions created beneath Knoop indentations. In this report we compare three varieties of commercially available polycrystalline SiC.

2. Experimental Procedure

The SiC materials tested were commercially obtained and included CoorsTek SiC-N, a pressure-assisted sintered material (CoorsTek Inc, Golden, Colorado), Saint-Gobain SiC-Hexoloy, a pressureless sintered material (Saint-Gobain Ceramics & Plastics Inc, Malvern, Pennsylvania), and Ekasic-T SiC-ESK, a liquid-phase sintered material (3M Technical Ceramics, Germany). These were obtained in the form of bend bars 50-mm long by 3 mm × 4 mm in cross section.

Samples to be indented were prepared by initially cutting the bars along the cross section into 3- × 4- × 3-mm pieces (length, width, height) using an ULTRA TEC ULTRASLICE precision saw (ULTRA TEC Manufacturing, Inc, Santa Ana, California) and a 150-μm-thick diamond blade running at about 5,000 rpm at the lowest feed-rate setting. With these conditions, the chipping at the edge of the sample from the sawing process was less than 20 μm. The surface to be indented was then polished flat to a specular finish using a series of diamond films with the last film being 1 μm grade. With the long axis of the Knoop indenter oriented perpendicular to the prepared cross section, a linear array of 10–12 indents were made on the polished surface with the centers at approximately 100 μm from the cut face. Indents were made using a Wilson Instruments' Tukon 2100 microindenter with a diamond indenter tip (Wilson Instruments, Norwood, Massachusetts). A loading of 1 kg was applied with a process time of 15 s, which resulted in Knoop indents approximately 8 μm × 80 μm.

Cross sections of the areas suitable for TEM analysis on the indented samples were then prepared by a multistep method[24] using a Leica TIC-3X (Leica Microsystems, Wetzlar, Germany) masked-ion milling system (MIMS), vacuum epoxy infiltration, and an FEI Nova 600 NanoLab focused-ion beam (FIB) mill (FEI Company, Hillsboro, Oregon). An added benefit of the multistep preparation technique was the ability to examine the cross section of the indents in the scanning electron microscope (SEM).

After the MIMS process and prior to the infiltration step, the indents for each sample were examined and indexed using a Hitachi S-4700 SEM (Hitachi America, Ltd, Tarrytown, New York). This step allowed selecting the indents that were closest to being cut at the midpoint of the indent long axis and assessing the quality of the cross section prior to the epoxy covering up the indent. The indexing was performed by aligning the edge of the cross section with one of the axes of the SEM and then measuring the distance from a corner of the sample to the indent by using the X-Y position values of the SEM stage as illustrated in Fig. 2. Tilting the sample to 45° in the SEM permitted both the cross section and the top indented surface to be imaged simultaneously. In the FIB, the distance from a corner was used to find

a particular indent even though it was obscured by the epoxy. This was accomplished by aligning the edge of the sample with the X-axis, finding the corner, and then doing a relative translation of the X-axis by the distance determined in the SEM. During the SEM examination for a particular indent, the extent of subsurface cracking seen determined the size of the TEM sample to be prepared by the FIB. The inherent microstructure was also examined by preparing TEM specimens of unindented SiC samples. These samples were prepared by standard dimpling and low-angle and low-energy argon (Ar) ion milling in a Gatan PIPS II ion mill (Gatan Inc, Pleasanton, California).

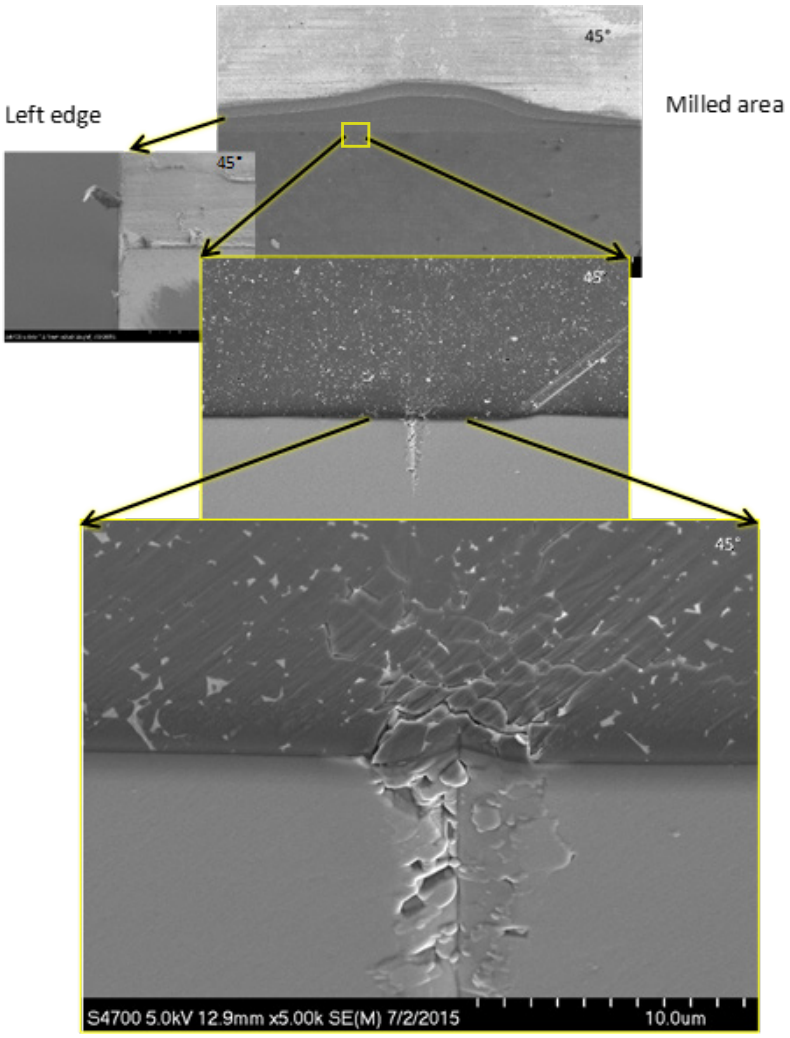

Fig. 2 SEM images of an indented SiC sample at different magnifications showing the procedure for indexing the indents

Imaging was done using a JEOL 2100F (JEOL USA Inc, Peabody, Massachusetts) TEM/STEM (scanning transmission electron microscope) equipped with Gatan DigitalMicrograph and DigiScan systems and an Oxford Instruments (High

Wycombe, United Kingdom) INCA energy-dispersive X-ray spectroscopy (XEDS) system. Spectrum imaging used the XEDS signal in area or line profile modes and was primarily used to determine the chemical nature of the included phases. Multivariate statistical analysis (MSA) of the spectrum images was performed using the Interdisciplinary Centre for Electron Microscopy (CIME) (Lausanne, Switzerland) MSA/principal component analysis plugin for Gatan DigitalMicrograph or the Automated eXpert Spectral Image Analysis (AXSIA) program (Sandia National Laboratories, Albuquerque, New Mexico).[25–27]

3. Results and Discussion

3.1 As-Received SiC

The initial comparison of unindented samples showed some obvious differences between the three materials—namely, grain size, defect densities, and phase distributions. The largest grain size was observed in the SiC-Hexoloy and SiC-N materials, which were approximately equal, having grain sizes averaging 5–10 μm. The average grain size for the SiC-ESK was much smaller at about 0.5–1 μm. Figure 3 shows representative SEM images of the three materials at the same magnification, while Fig. 4 shows representative bright-field (BF) TEM images of the three materials that further illustrates the differences in grain size. The larger grain size for SiC-N is due primarily to the larger initial powder particle size (~5 μm). Because SiC-Hexoloy is pressureless sintered, its initial powder particle size is on the order of approximately 1 μm. However, even with sintering aids and a fine initial powder particle size, pressureless sintering requires high processing temperatures of approximately 2200 °C to achieve full densification. Consequently, grain growth occurs, resulting in a significant increase in grain size. Liquid-phase sintered SiCs are typically processed with approximately 7–8 volume percent yttrium aluminum garnet (YAG) at temperatures between 1900–2000 °C. At these temperatures, YAG is a liquid phase, which wets the SiC particles and through particle rearrangement, capillary pressure, and solution–reprecipitation, densifies the initially porous (“green”) body. For this process to be successful, the initial particle size is typically also fine, like in pressureless sintering. This particle size allows for high green densities to be achieved and relatively low oxygen contents (oxide surface particle coatings). The high curvatures associated with relatively fine pore channels and particles allow for large capillary forces to develop, thus promoting densification. During the solution–reprecipitation stage, some small amount of particle or grain growth is expected. The consequence is a fully dense ceramic with fine grain size. Interestingly, the solution–reprecipitation process can result in the formation of a “core-rim” type structure for the resulting

grains because of higher solute concentrations within the liquid that get incorporated into the SiC that is precipitating onto the surface of larger particles. Consequently, it is not surprising that the liquid-phase sintered SiC-ESK ceramic has not only the smallest grain size of the three SiC variants, but also a core-rim grain structure. This is evident in the SEM image of Fig. 3C. The SiC-N ceramic also possesses a core-rim grain structure suggesting the possible existence of a liquid phase during densification. This is evident in Fig. 3B.

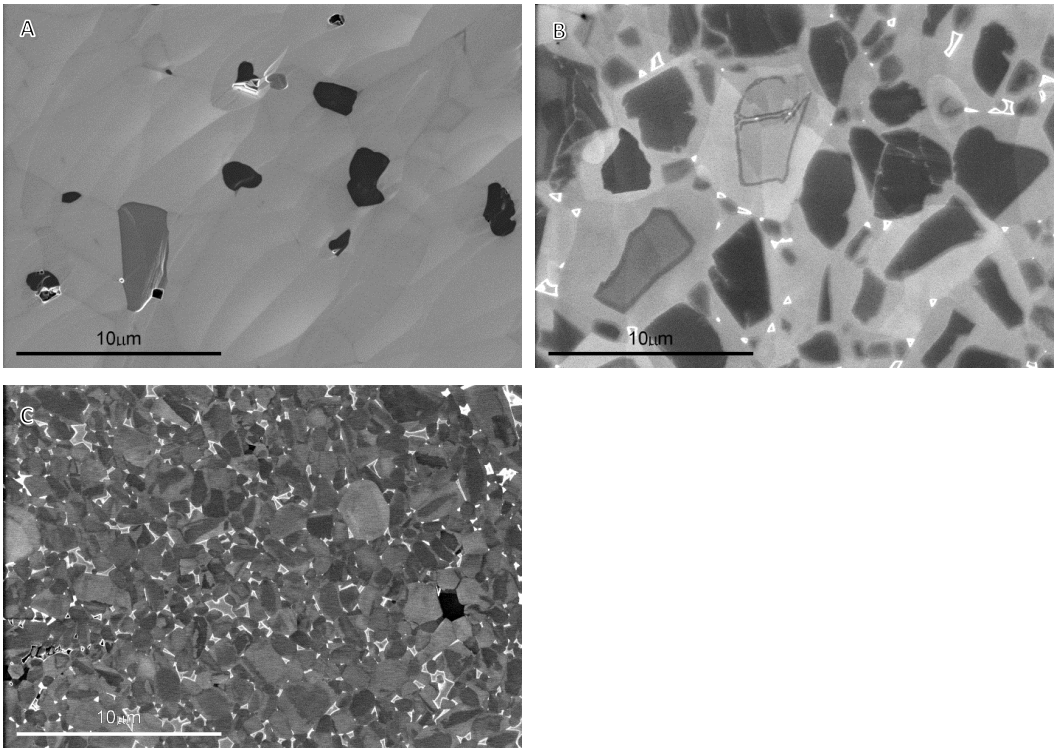

Fig. 3 SEM images showing relative grain size comparison: A) SiC-Hexoloy: 5–10 µm, B) SiC N: 5–10 µm, and C) SiC-ESK: 0.5–1 µm

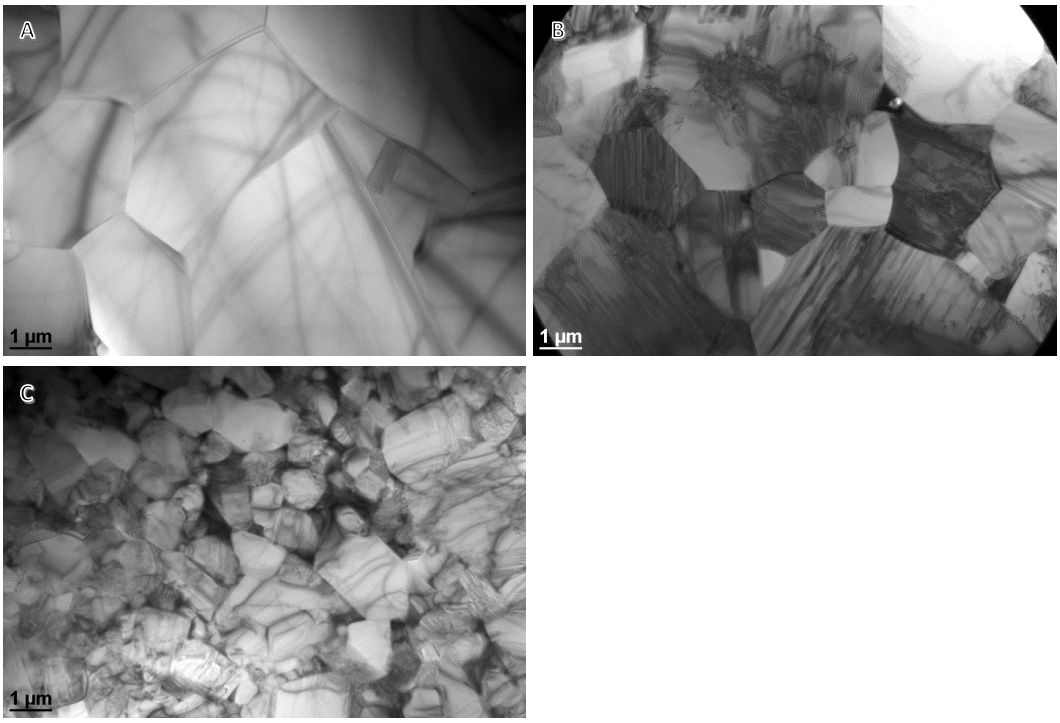

Fig. 4 TEM-BF images showing relative grain size comparison: A) SiC-Hexoloy: 5–10 µm, B) SiC N: 5–10 µm, and C) SiC-ESK: 0.5–1 µm

A qualitative examination of defects inherent in the three variants shows a combination of stacking faults, dislocations, and even a few twins. SiC-Hexoloy and SiC-ESK had the fewest preexisting defects while SiC-N contained the most, as shown in the BF TEM images in Fig. 5. It is presumed that the high pressure exerted during densification for the SiC-N produces a high defect density in that material.[28,29] The high stacking fault density in the SiC-N also indicates the numerous SiC polytypes that are present in that material compared to the other two.

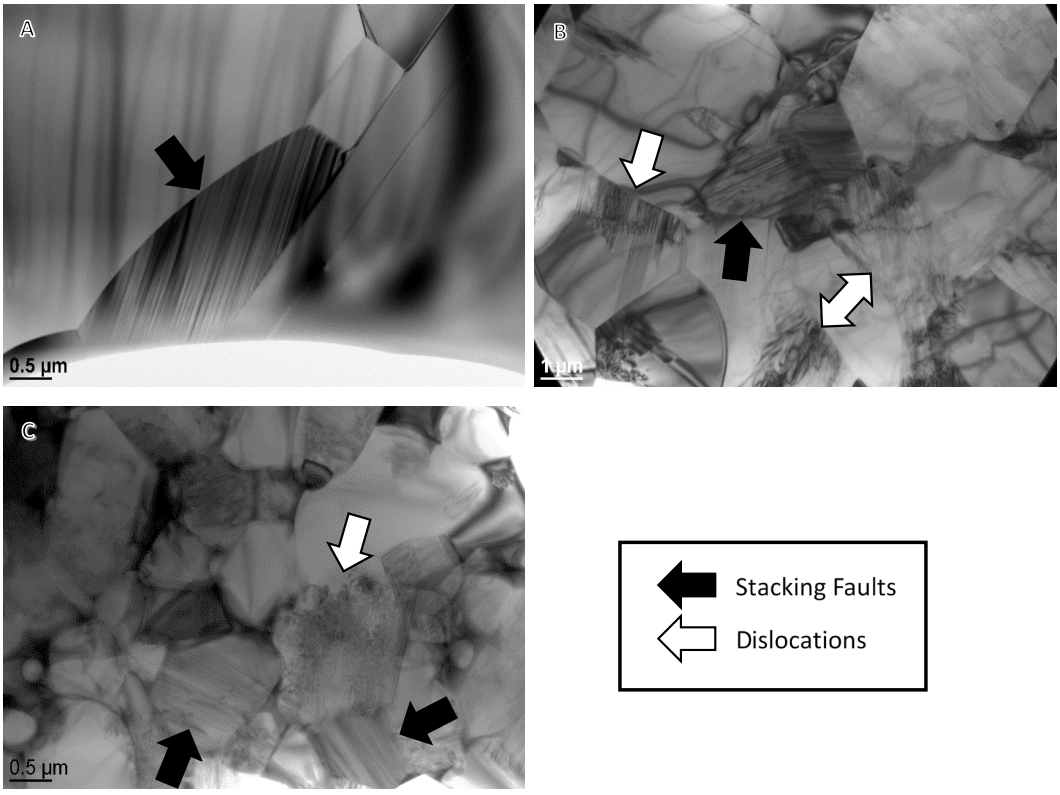

Fig. 5 TEM-BF images showing defects for A) SiC-Hexoloy: stacking faults and a single twin with most grains free from defects, B) SiC-N: stacking faults, twins, and dislocations, and C) SiC-ESK: stacking faults and second phases that are mostly intergranular

High-angle annular dark-field (HAADF) imaging in STEM mode clearly showed the distribution of second phases in these materials because the contrast is sensitive to the average atomic number. In all of the materials, tungsten carbide (WC) particles could sometimes be found in the images. This is due to the physical grinding of the powders before sintering. Because they do not affect the property of SiC in any significant way, no images with WC inclusions are shown for any of the SiC samples. These particles are small, limited in quantity, well dispersed and are usually seen at triple junctions. Figure 6 shows STEM BF, dark field (DF), and HAADF images from SiC-Hexoloy that show one of these sparse inclusions of graphite and a few smaller oxide inclusions. The volume fraction of these inclusions is very low in this material and does not influence its mechanical properties. Figure 7A shows a spectrum image line profile across the graphite inclusion shown in Fig. 6. Graphite is the most common inclusion found in this material, but graphite has been detected in all of the SiC types. Figure 7B shows the grayscale line profile of the HAADF signal. MSA analysis identifies additional inclusions within the graphite inclusion. The profile for the SiC component phase is seen in Fig. 7C, while the graphite component profile is seen in Fig. 7E. Within the graphite phase,

a presence of Ar is seen (Fig. 7F). This is most likely an artifact from the ion milling during TEM preparation. Additionally, Fig. 7D shows the presence of an oxide phase adjacent to the graphite phase with complicated chemistry that includes zirconium (Zr), iron (Fe), chromium (Cr), vanadium (V), and titanium (Ti) whose origin is unknown. Figure 8A shows a spectrum image line profile of another metalloid inclusion found at a triple junction in SiC-Hexoloy. MSA analysis reveals that there are three spatial components: the matrix SiC phase shown in Fig. 8C and two adjacent and overlapping metalloid phases. Figure 8D shows a silicon (Si)-rich phase with minor amounts of Zr and Fe that overlaps within the thickness of the sample phase in Fig. 8E, which is Si- and Fe-rich with no Zr seen. The MSA data also show that the phase in Fig. 8E overlaps with the matrix within the sample thickness.

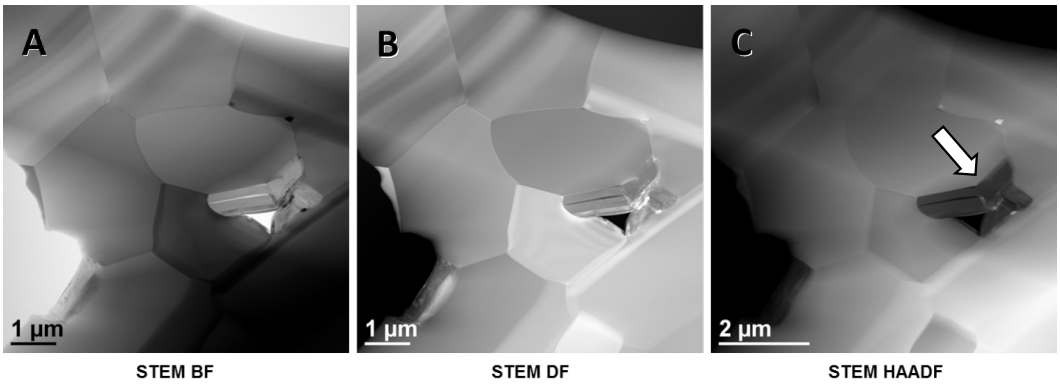

Fig. 6 SiC-Hexoloy: A) STEM BF, B) STEM DF, and C) STEM HAADF images showing a graphite inclusion (arrow) containing a few smaller oxide inclusions

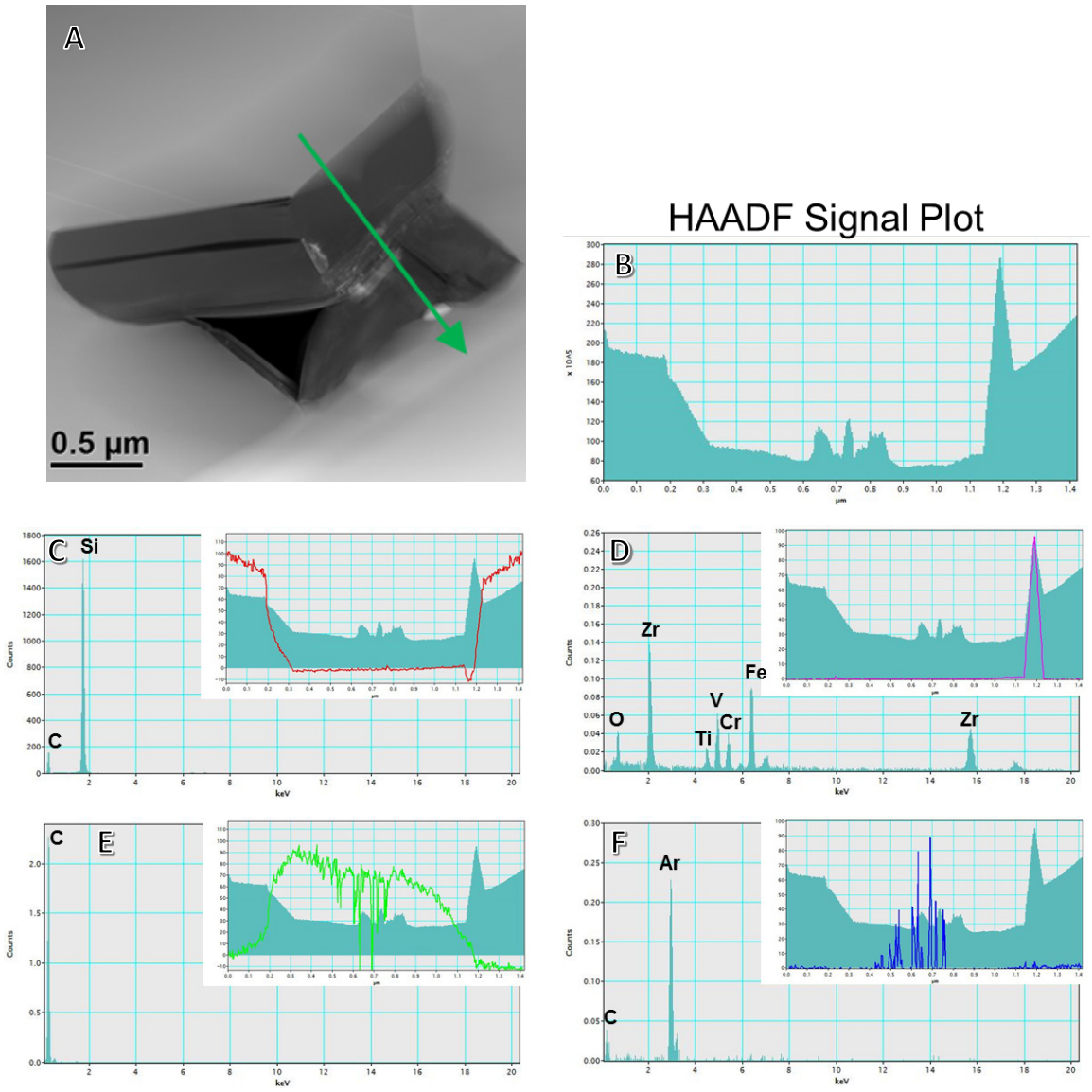

Fig. 7 A) XEDS spectrum image data acquired across graphite inclusion from Fig. 6. B) The HAADF signal plot shows the intensity across the line profile and is superimposed on four distinct spatial components (C, D, E, F) as determined by MSA analysis.

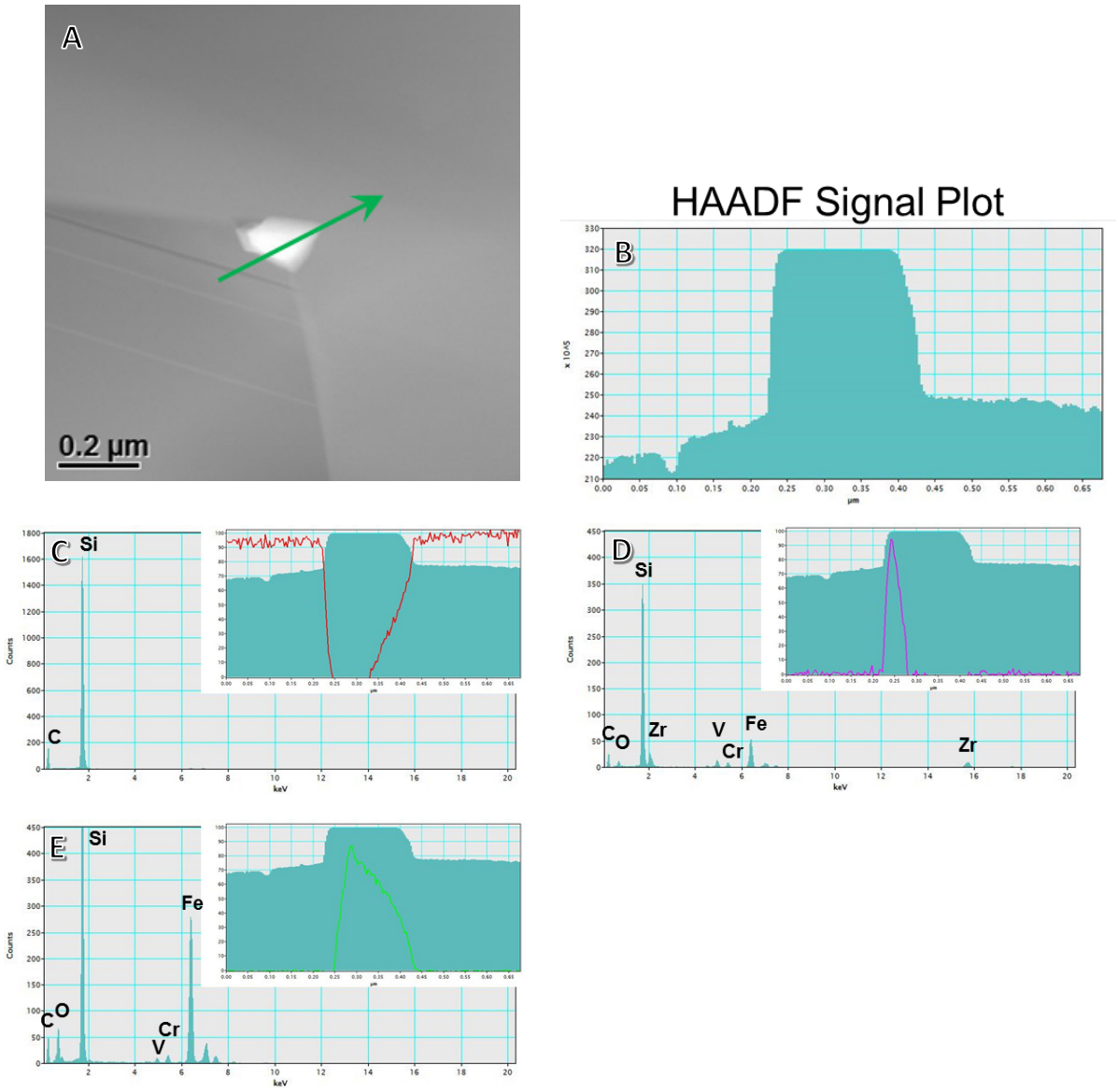

Fig. 8 A) XEDS spectrum image data acquired across inclusion in SiC-Hexoloy at a triple junction. B) The HAADF signal plot shows the intensity across the line profile and is superimposed on three distinct spatial components (C, D, E) as determined by MSA analysis. There are two phases present: a SiC (C, E) and a metalloid (D, E). E) indicates that the inclusion overlaps part of the SiC matrix.

With the high defect density and crystalline secondary phases, it is difficult to differentiate the included phases in SiC-N when viewed in TEM-BF from the matrix as shown in Fig. 9A and B. The reason for this is that diffraction contrast coupled with the increased strain contrast from defects dominates in the images while the mass differences add little to the contrast. Although diffraction contrast is still dominant in the STEM-BF image of Fig. 9C, the strain contrast is significantly reduced and this helps differentiate the second phase (indicated with an arrow) from the SiC matrix. However, with the Z-contrast imaging of STEM-

HAADF, the indicated phase is more easily identified as shown in Fig. 9D. The SiC-N material has a variety of different phases. Graphite is also seen in this material. Figure 10 shows an MSA analysis of an XEDS spectrum image of an area that shows several phases. The analysis shows the prevalence of an Al-Si-rich oxide phase and another Al-Si oxide with a high concentration of Fe. The presence and distributed volume fraction of these Al-Si-rich oxide phases are thought to be responsible for giving SiC-N mixed grain boundary complexions. A grain boundary complexion is a structure of the grain boundary that may or may not include an intergranular film and behaves similar to a phase in that it can undergo transformations at different temperatures in a similar fashion as equilibrium phases in a bulk.[30] Approximately half of the grain boundaries observed in SiC-N have an intergranular film.[31] Figure 11 shows an approximately 10-nm-thick intergranular Al-Si-oxide film in SiC-N analyzed by MSA, while Fig. 12 shows another grain boundary that is clean. The grain boundaries that were characterized were ones that were oriented parallel to the X-tilt axis of the specimen holder. To further improve the dimensional accuracy of the width of the grain boundary, the sample was tilted to minimize its appearance in STEM-BF mode. Figure 13 shows a line profile across another grain boundary that shows an intergranular film. It is interesting to note that Fig. 12 has a second phase at a triple junction for the grain boundary analyzed, but no intergranular film is present; while in Fig. 13, no second phase is seen but an intergranular film is present. In SiC-N, these different grain boundary complexions, particularly the presence of thin intergranular films at about half of the grain boundaries, are thought to improve fracture toughness as well as impact performance.

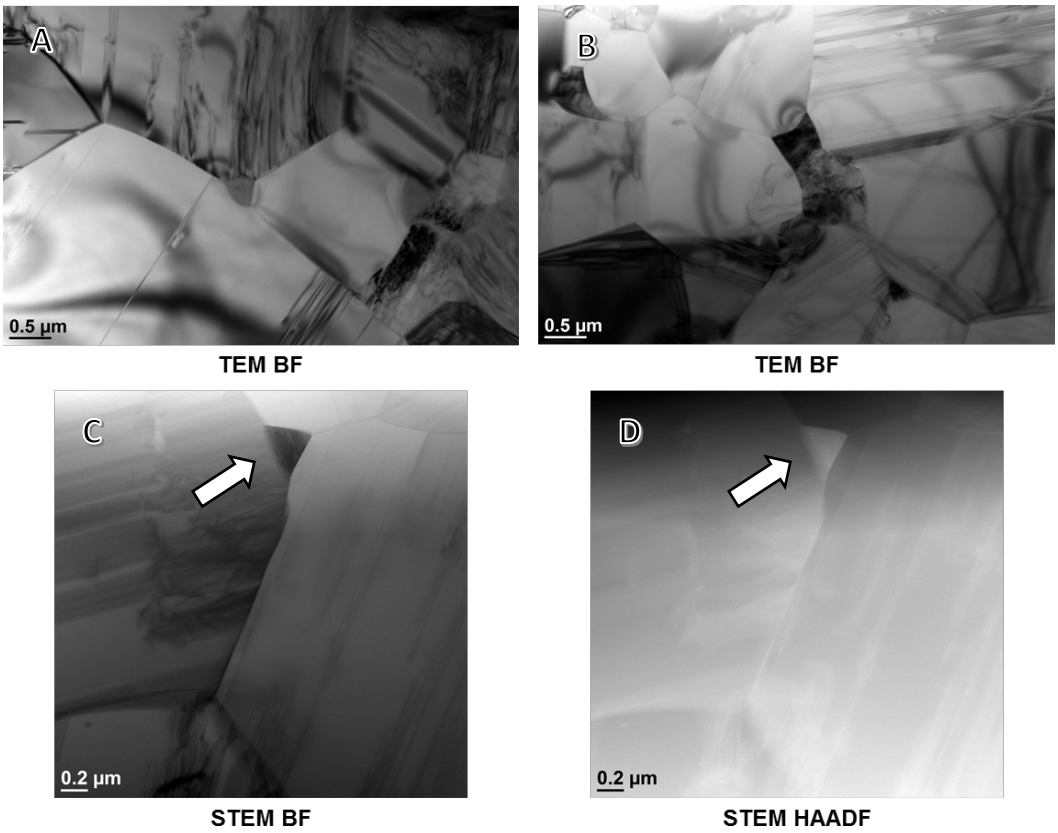

Fig. 9 BF-TEM images A) and B) of SiC-N showing that it is difficult to differentiate the matrix from secondary phases using diffraction contrast. C) STEM-BF and D) STEM-HAADF are images of an oxide phase (indicated by arrow) showing that it is easier to determine the presence of secondary phases.

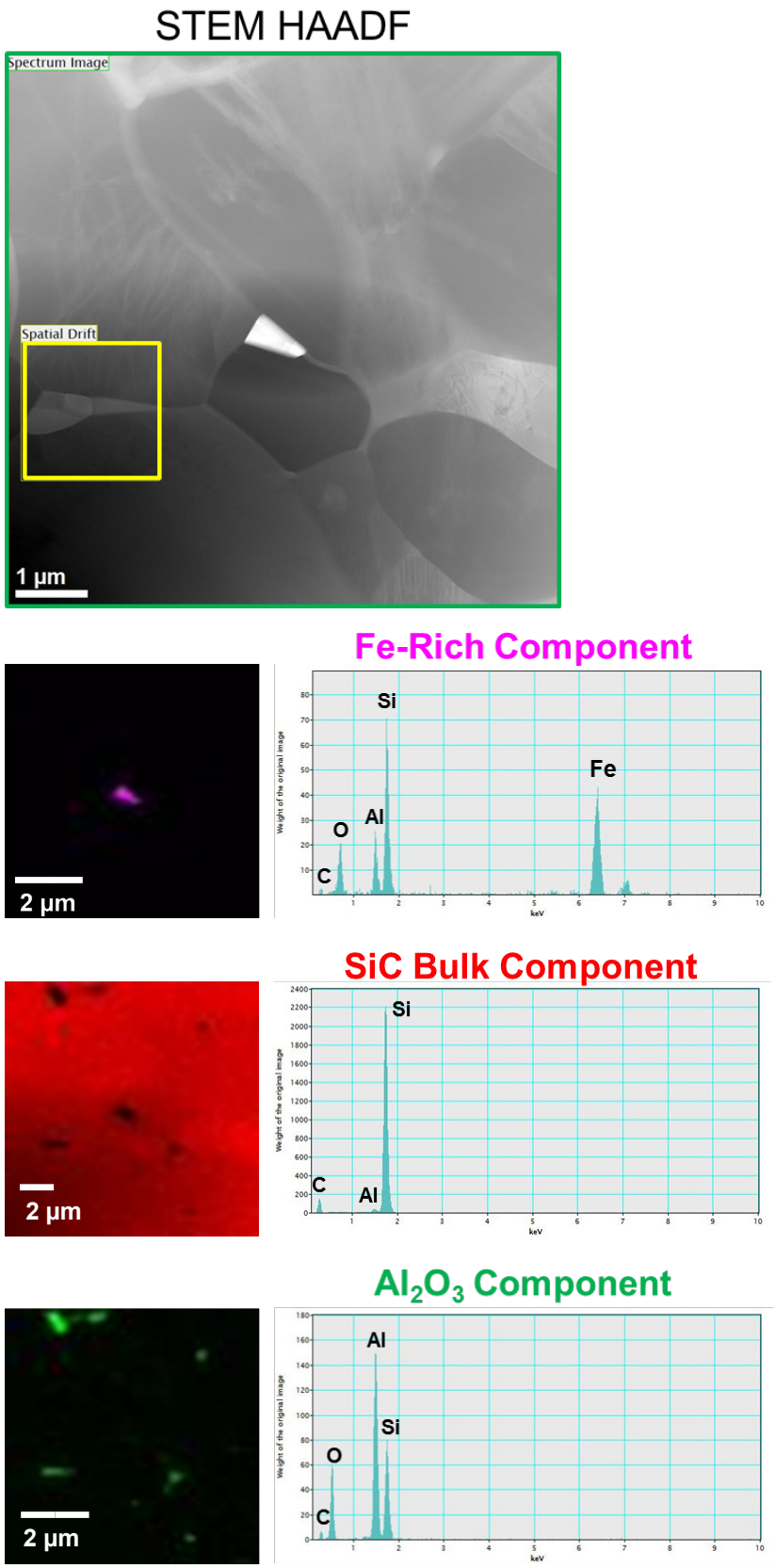

Fig. 9 MSA analysis of an XEDS spectrum image area of SiC-N with several phases seen. (Yellow box in lower left of top image used for drift correction reference.)

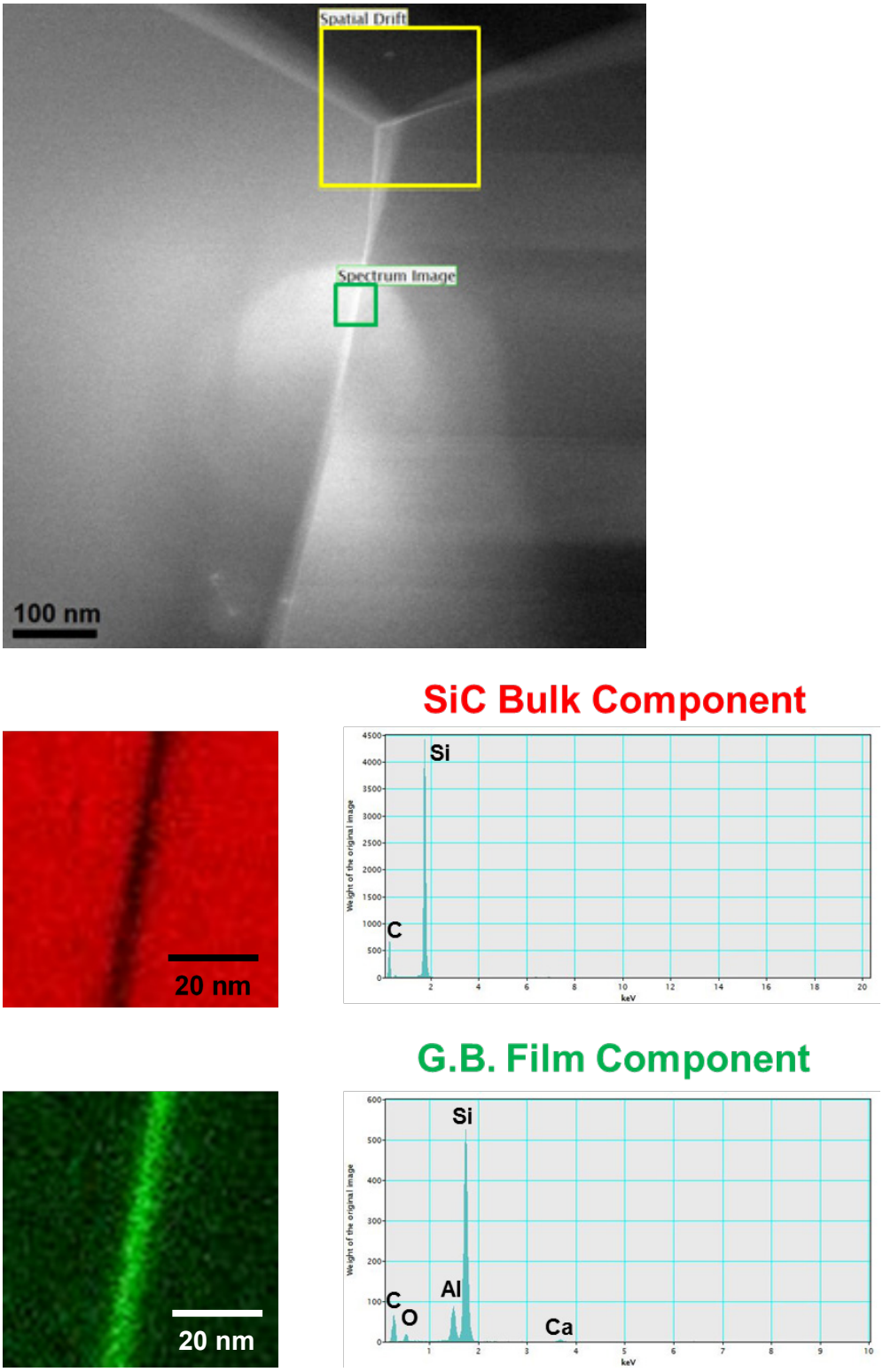

Fig. 10 MSA analysis of an XEDS spectrum image of a grain boundary (G.B.) in SiC-N (denoted by green box in top image) showing about a 10-nm-thick intergranular film. (Yellow box in upper right image used for drift correction reference.)

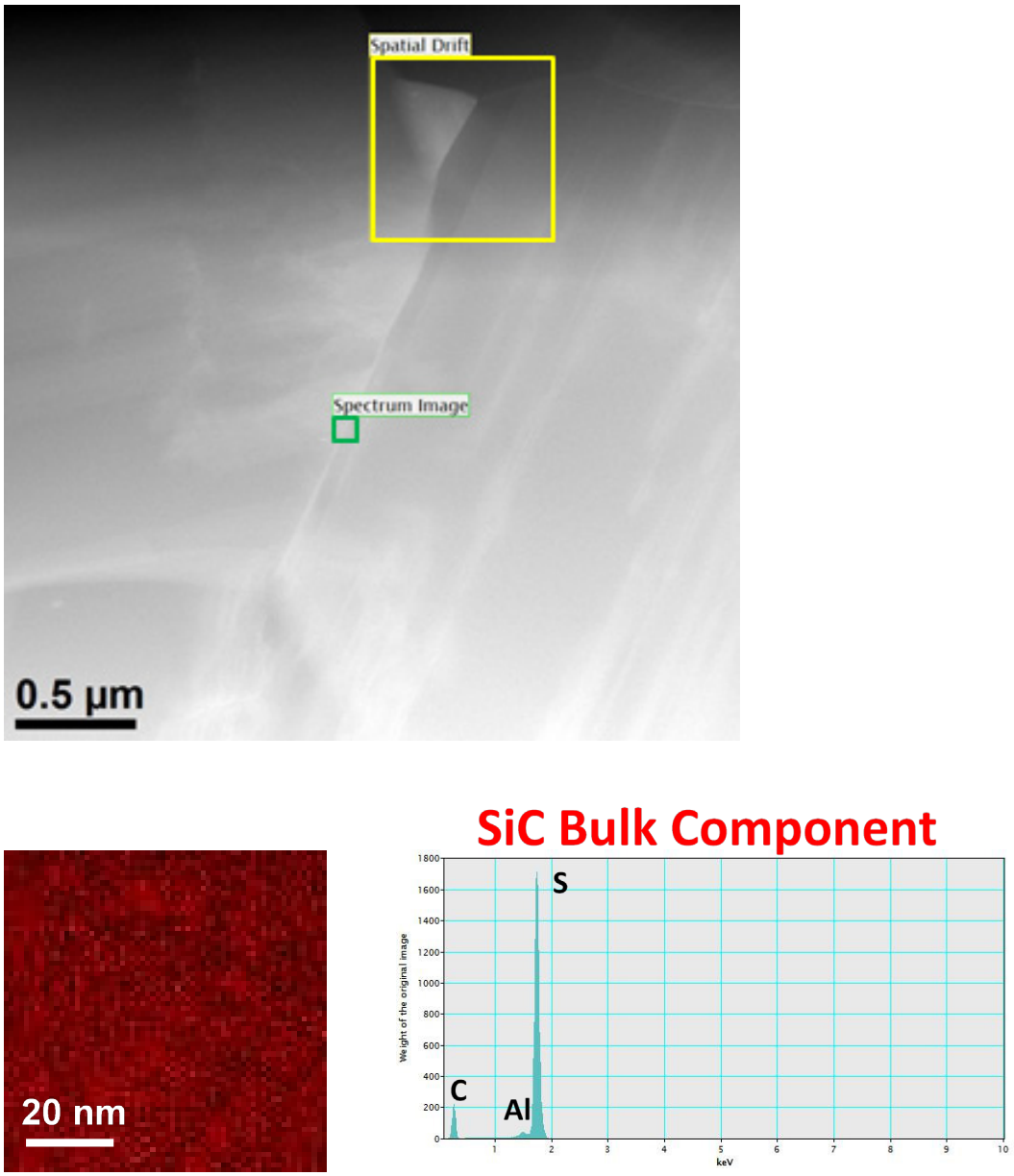

Fig. 11 MSA analysis of an XEDS spectrum image of a clean grain boundary in SiC-N (denoted by green box in upper image) showing no intergranular film present. (Yellow box in upper right of top image used for drift correction reference.)

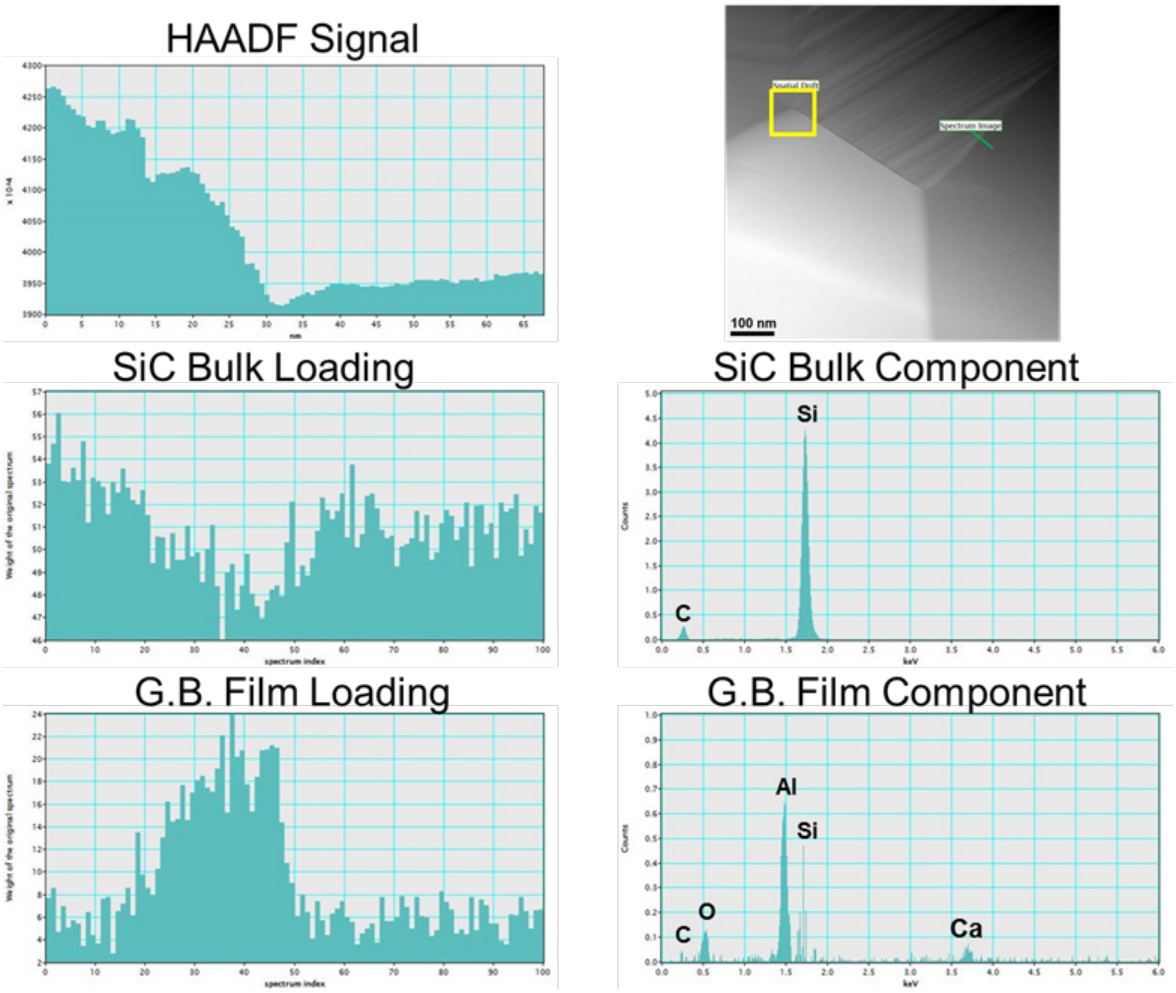

Fig. 12 MSA analysis of an XEDS spectrum image line profile (green line upper right image) of a grain boundary showing a thin intergranular film in SiC-N. (Yellow box in upper right image used for drift correction reference.)

The SiC-ESK microstructure contains many grains completely wetted by thicker intergranular phases and films. It is this film that forms the liquid in the liquid-phase sintering of this material. Figure 14 shows an area of SiC-ESK that has a glass phase in the triple junctions of grains and a thick film that fills in between grains. For the most part, these phases are amorphous. Figure 14A is a TEM-BF image that shows the pronounced strain contrast present that obscures some microstructural details such as the indicated dislocations. Much of the strain contrast seen in the BF images is removed in the STEM-BF image (Fig. 14B) and the STEM-DF image (Fig. 14C), which allows clearer images of the dislocations. But the Z-contrast of the intergranular phase and the films along grain boundaries is clearly seen in the STEM-HAADF image (Fig. 14D). The relative distribution of these intergranular phases is demonstrated in Fig. 15, which shows spectra collected from four points within different phases. It is easily seen that there are different

chemistries of the Y-Al-rich, Al-rich, and Si-rich oxide phases. The phases can readily be seen at triple points and "filling" in between grains. The intergranular films that can be seen between grains along the boundaries will originate from these junction phases. This was clearly seen in Fig. 14.

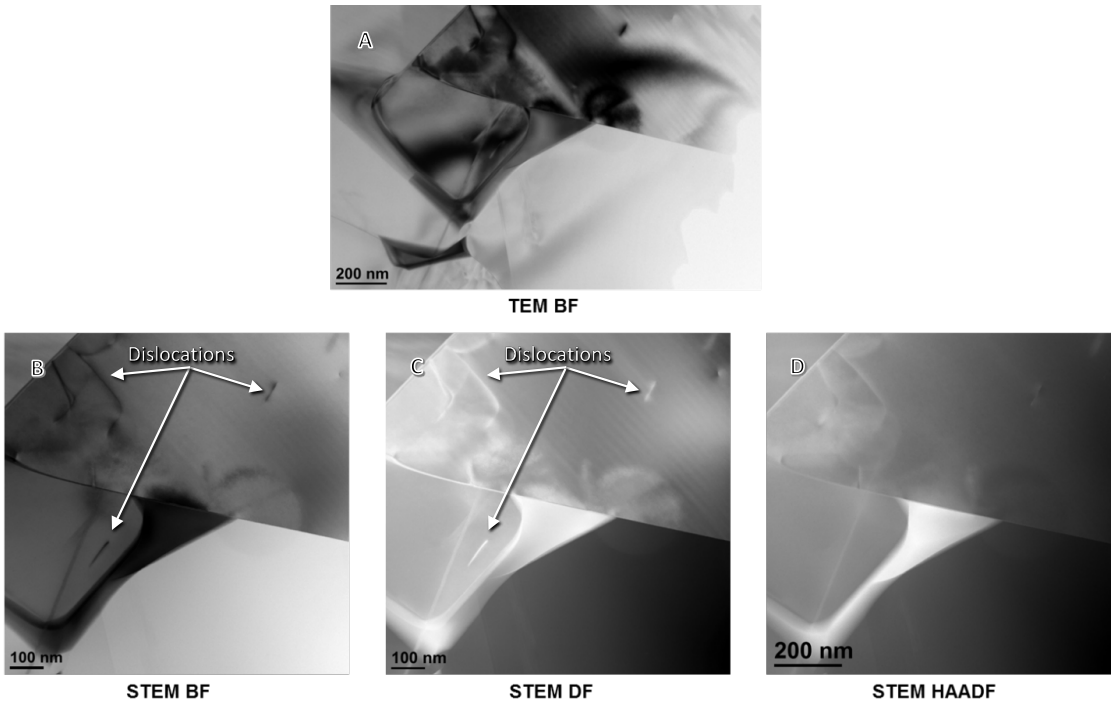

Fig. 13 Images of SiC-ESK: A) TEM-BF, B) STEM-BF, C) STEM-DF, and D) STEM-HAADF. Removal of the strain contrast in A) allows dislocations to be more easily observed with B) STEM-BF and C) STEM-DF.

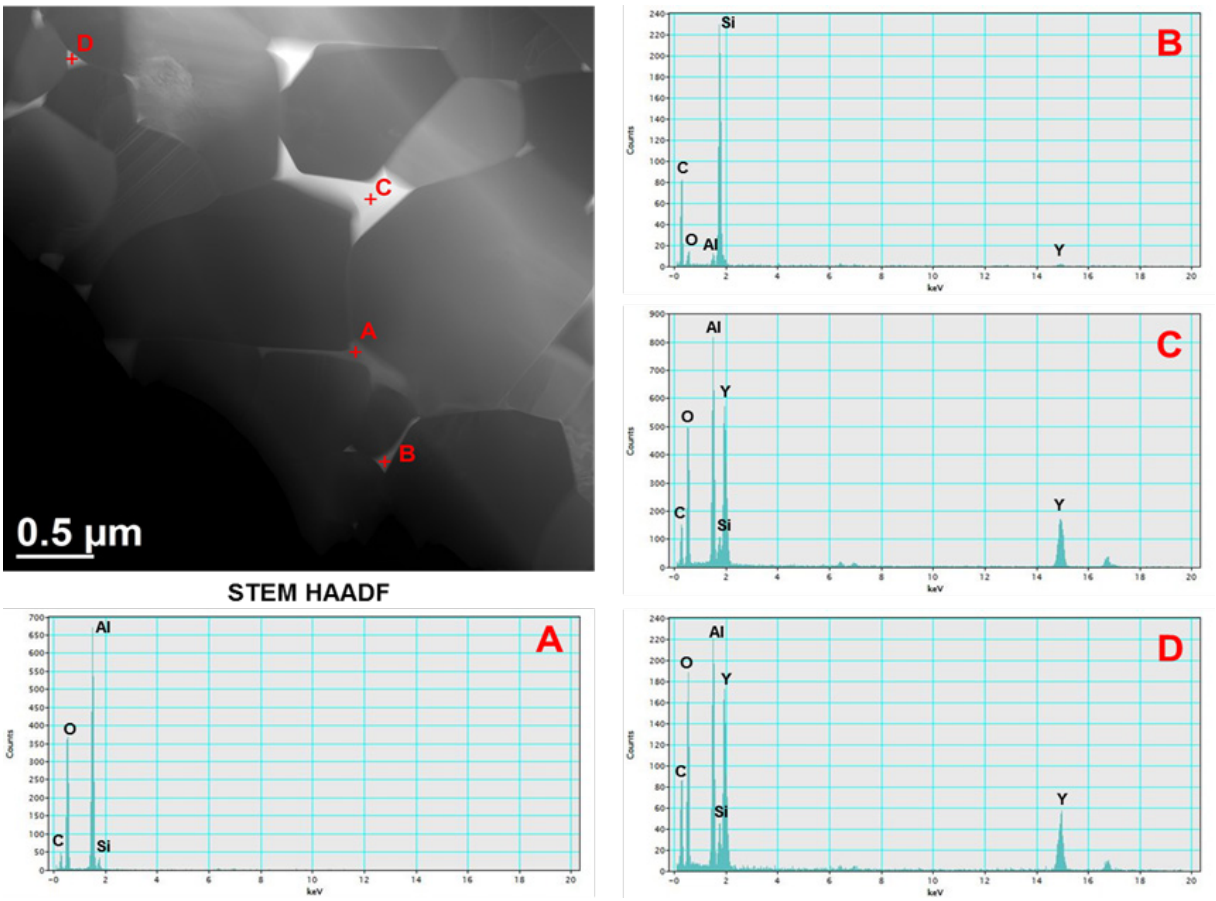

Fig. 14 STEM-HAADF image of SiC-ESK along with XEDS analysis at four points within intergranular phases

3.2 Indented SiC

The multistep sample preparation technique that was developed for indented SiC samples allowed the full extent of the inelastic region under the indents to be preserved and fully examined in the TEM as demonstrated in Fig. 16.[32]

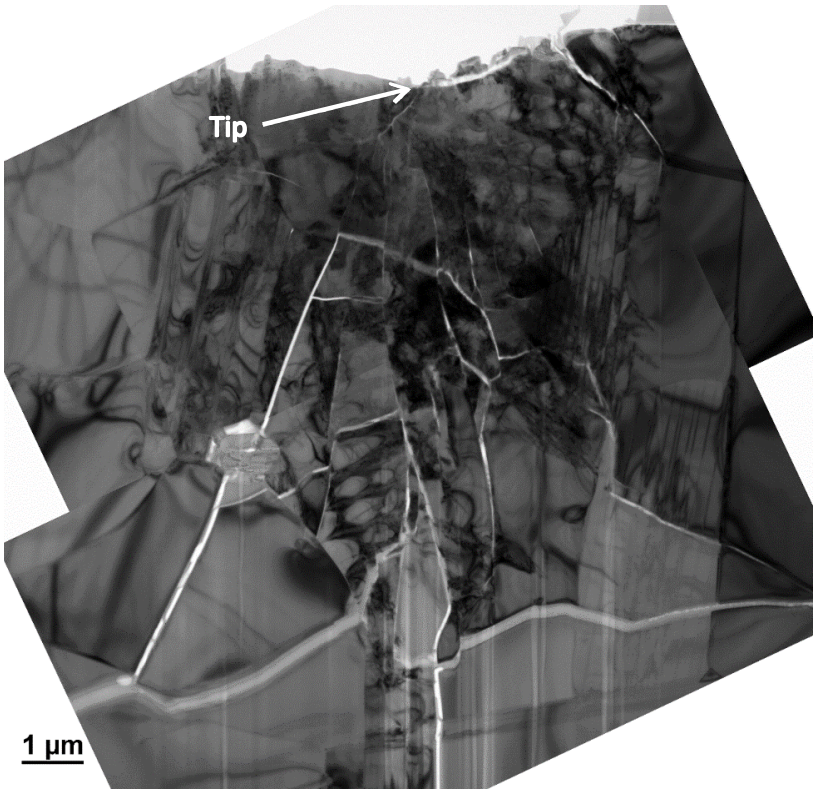

Fig. 15 Low magnification TEM-BF montage showing the extent of the inelastic region of the 1-kgf indent in SiC-Hexoloy

To be consistent with discussion of the as-received SiC, the indented SiC materials will be discussed in the same order as the as-received materials. There were some common features of the indented SiC samples. These included intergranular and intragranular cracking, the increased density of stacking faults, the generation of dislocations, and the observation of shear bands. Severe intergranular cracking was immediately obvious in SiC-N and SiC-ESK. Figure 17 shows relatively low magnification STEM-HAADF images of the region just below the indent of the three SiC materials. Because the epoxy has a lower average atomic number than the SiC and other included phases, the HAADF images clearly show both the intergranular and the intragranular cracks that occur in these materials. Because the tip of the indent at the surface was preserved and the whole extent of the inelastic region was revealed, as shown in Fig. 16, microstructural defect features and the amount of deformation could be determined relative to the distance from the tip of the indent. This could then be correlated to theoretical strain calculations, if desired. Figure 18 shows the benefit of imaging with STEM-BF compared to TEM-BF. STEM-BF decreases strain contrast in the image and certain crystalline defects, such as dislocations, can be seen more clearly. In all the samples, shear bands could be located that showed steps where the band would meet the surface of an intergranular crack in SiC-ESK, as shown in Fig. 19.

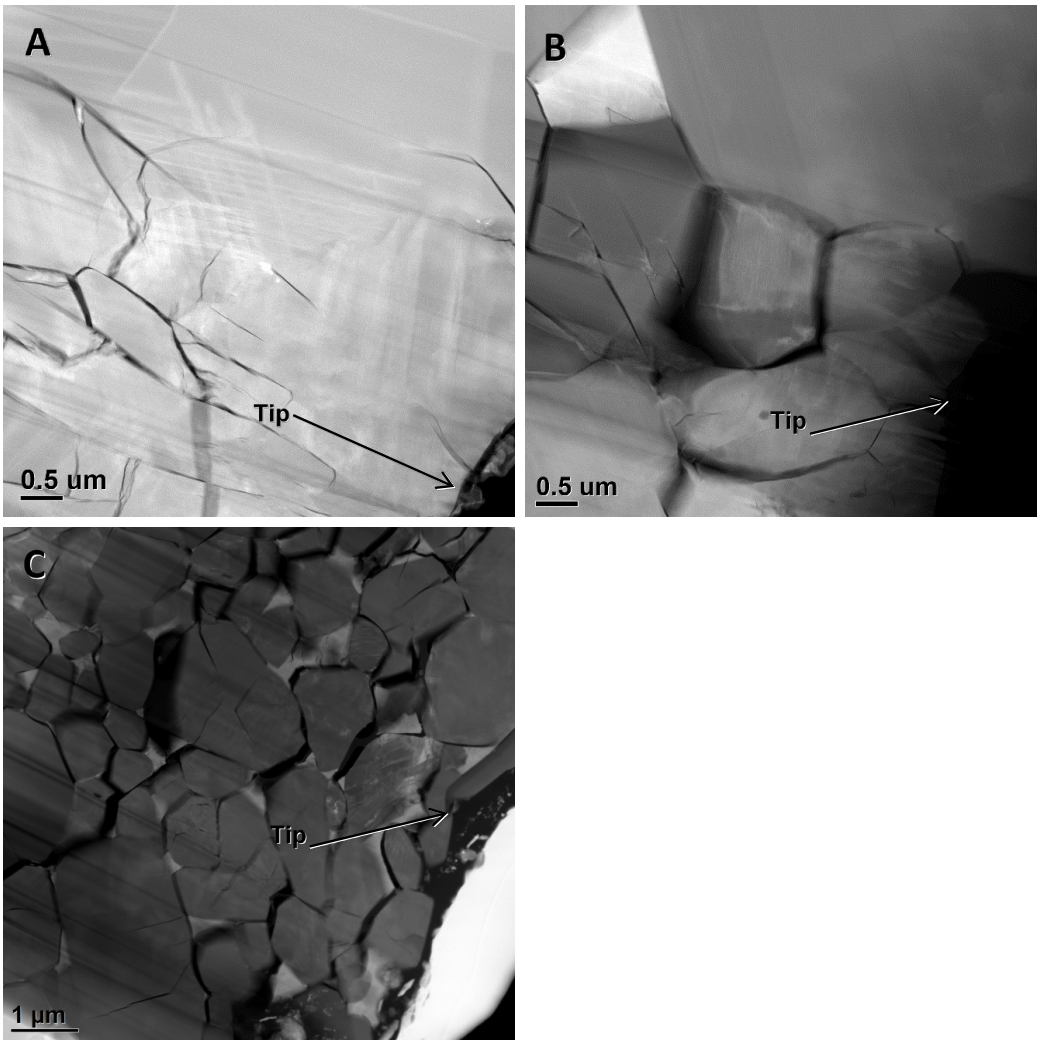

Fig. 16 STEM-HAADF images of the subsurface regions just below the indent in A) SiC-Hexoloy, B) SiC-N, and C) SiC-ESK. (Note the scale change.)

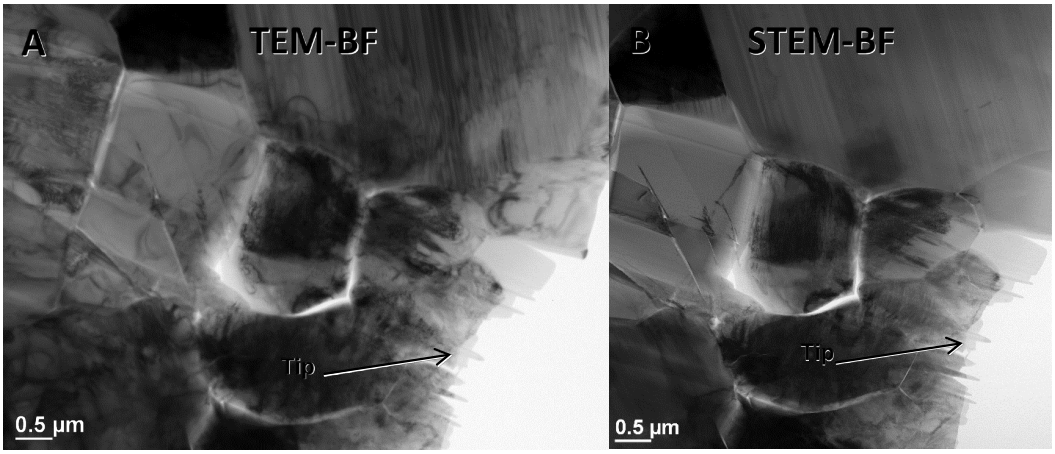

Fig. 17 A) TEM-BF image of SiC-N and B) STEM-BF image of the same area that shows decreased strain contrast

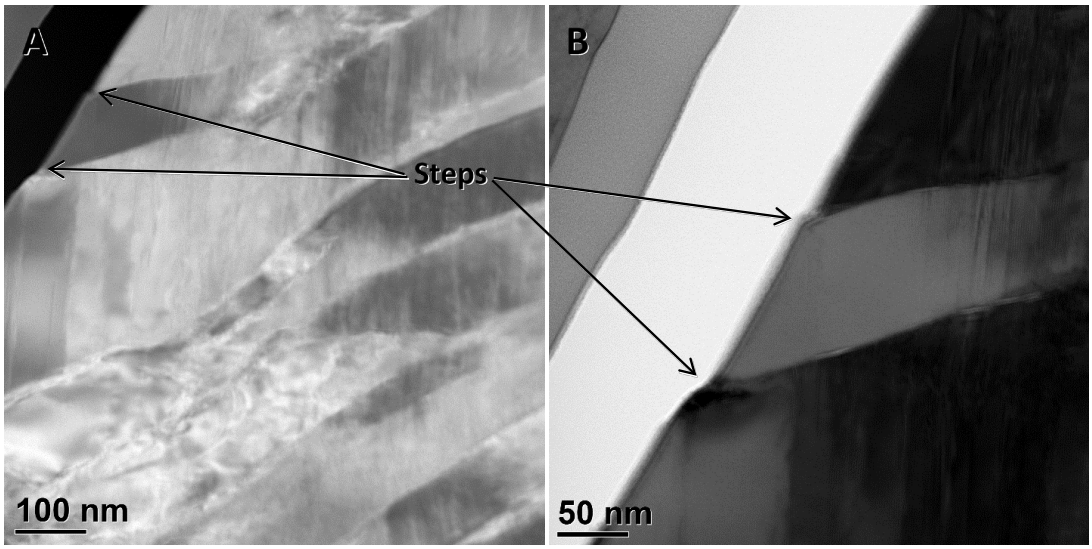

Fig. 18 A) STEM-DF image of shear bands in SiC-ESK; B) enlarged STEM-BF image of a shear band in A) at the crack surface showing two steps at the surface

The larger grain size of the SiC-Hexoloy material causes much of the cracking that occurs under the indent to be intragranular in nature (Fig. 20). The cracking both laterally and vertically can extend quite far from the indent, as shown in the very low-magnification image in Fig. 20A. The strain contrast from the increase in defect density is quite apparent in the inelastic zone. Stacking faults can be seen further from the tip of the indent, but the extreme strain, shown better in Fig. 21, is primarily due to a dislocation entanglement with such a high density of dislocations that it prevents individual dislocations from being seen.

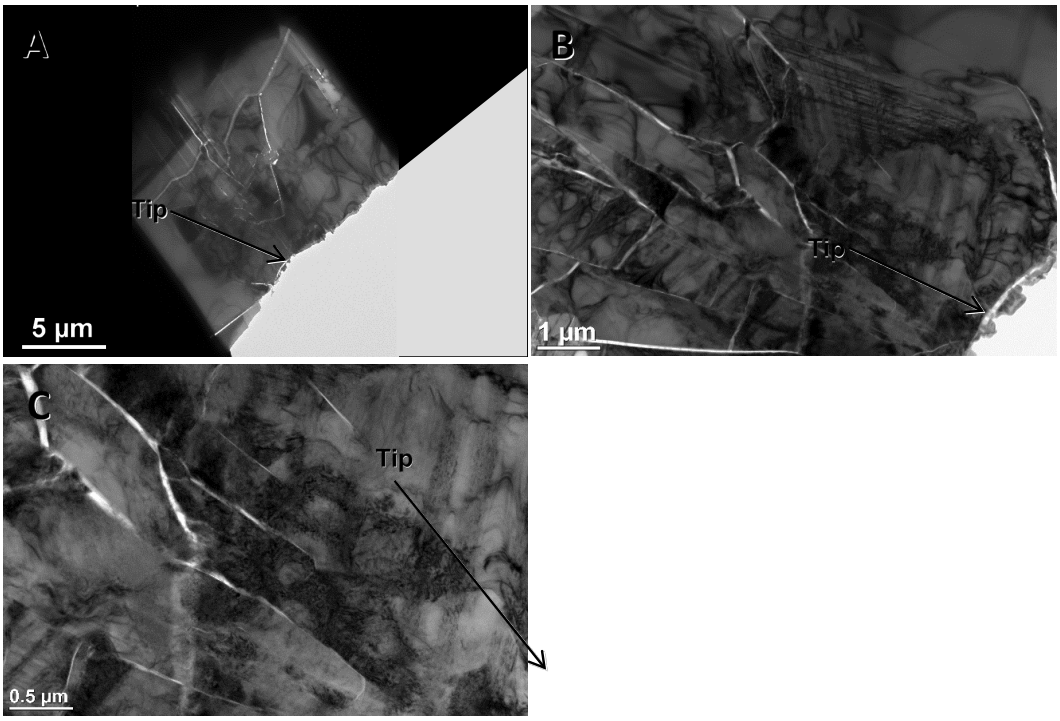

Fig. 19 A) Low-magnification TEM-BF image of SiC-Hexoloy, B) TEM-BF image showing that cracking is primarily intragranular in the inelastic zone beneath the indent, and C) higher magnifcation showing the high defect density in this area

Fig. 20 TEM-BF of SiC-Hexoloy showing the extremely high strain contrast due to the high defect density in the inelastic zone beneath the indent. The strain is primarily due to high dislocation entanglements.

The SiC-N material has a higher defect density in the as-received material than the other two materials and, because of that, it is nearly impossible to ascertain whether a defect such as a stacking fault or dislocation was preexisting. After indentation, both the dislocation and stacking fault densities are much higher in the inelastic

zone than were seen in the as-received SiC-N. As shown in Fig. 17, intragranular cracks can appear at triple junctions because of stress concentration. The increase in dislocations also seems to be concentrated around these types of sites (Fig. 22). It is obvious that these sites nucleate dislocations, which then move away under the applied stress. The grain boundaries near triple junctions within the inelastic zone also seem to show a higher concentration of stacking faults (Fig. 23).

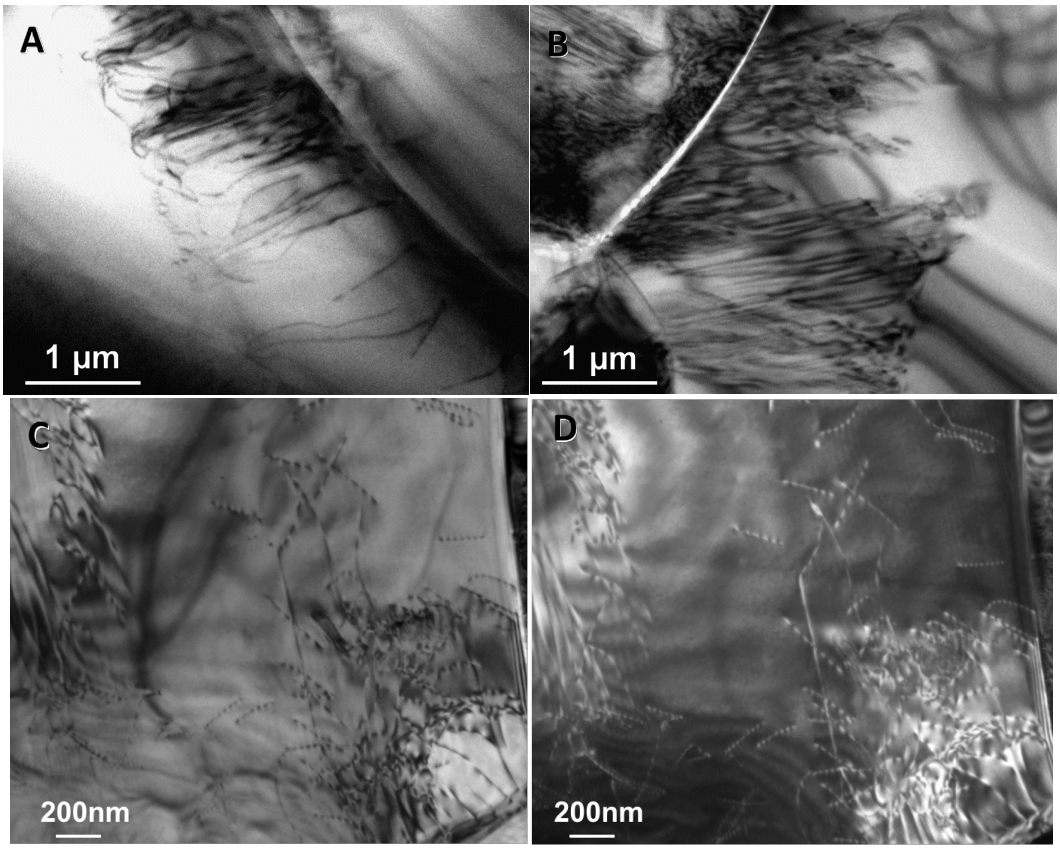

Fig. 21 TEM-BF images of dislocations associated with the high stress concentration sites at triple junctions in SiC-N (A, B, and C), and D) TEM-DF of C)

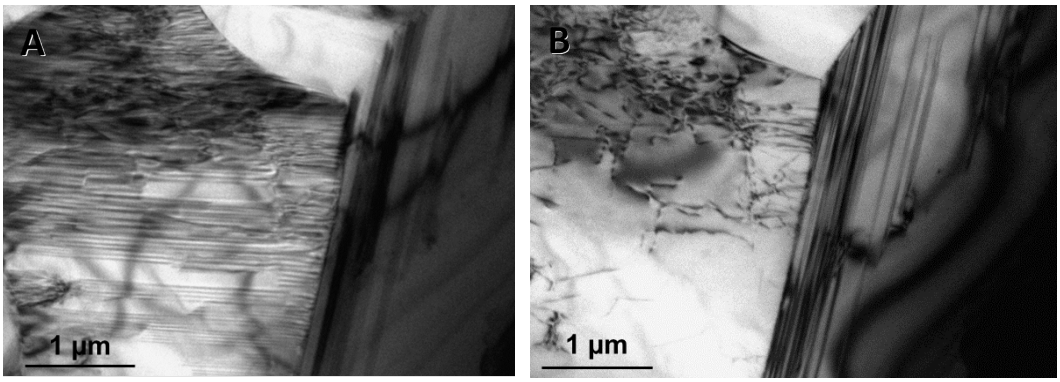

Fig. 22 A) and B) TEM-BF images of SiC-N showing the increased density of stacking faults that are associated with triple junctions in the inelastic zone

The behavior of the SiC-ESK materials is quite different than the other two SiC materials. Because of the oxide wetting films on the grain boundaries and the oxide particles at triple junctions, the intergranular cracking of the SiC-ESK follows the grain boundaries extensively. This can be seen in the very low-magnification TEM-BF image in Fig. 24. It is impossible to tell from the indented sample whether all of the observed intergranular cracking was due to the presence of an intergranular film because the thickness of the intergranular films in SiC-ESK varied from very thin to thick as shown in Figs. 14 and 15. Also, because of the smaller grain size in the SiC-ESK, there are more triple junctions that cause the stress concentration sites leading to intragranular cracking. This was seen clearly in the STEM-HAADF image in Fig. 17C. The inelastic region is not as well defined with the SiC-ESK material as it was for SiC-Hexoloy and SiC-N. This can be seen in the relatively low-magnification image shown in Fig. 25A. However, within the grains under the indent, the defect density, and hence the strain, is high, showing that plastic deformation is also occurring within the grains. This can be seen in Fig. 26A–C. The large dark grain in Fig. 26B is basally oriented and shows a high density of dislocations and stacking faults visible within that grain. Fig. 26B also shows the intergranular cracking in the other two grains adjacent to that dark grain.

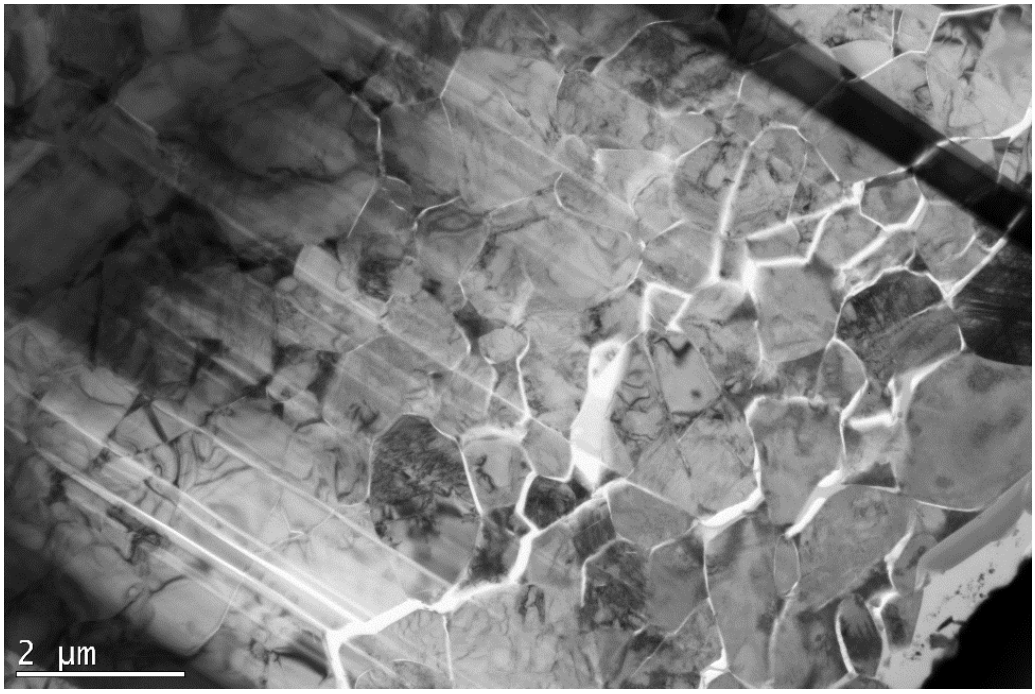

Fig. 23 Low-magnification TEM-BF image of SiC-ESK under the indent

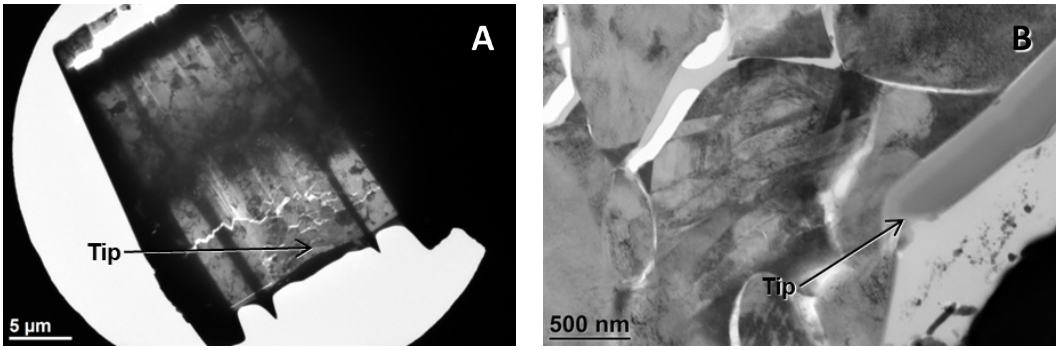

Fig. 24 TEM-BF images of SiC-ESK showing location of indent tip: A) low magnification, and B) higher magnification

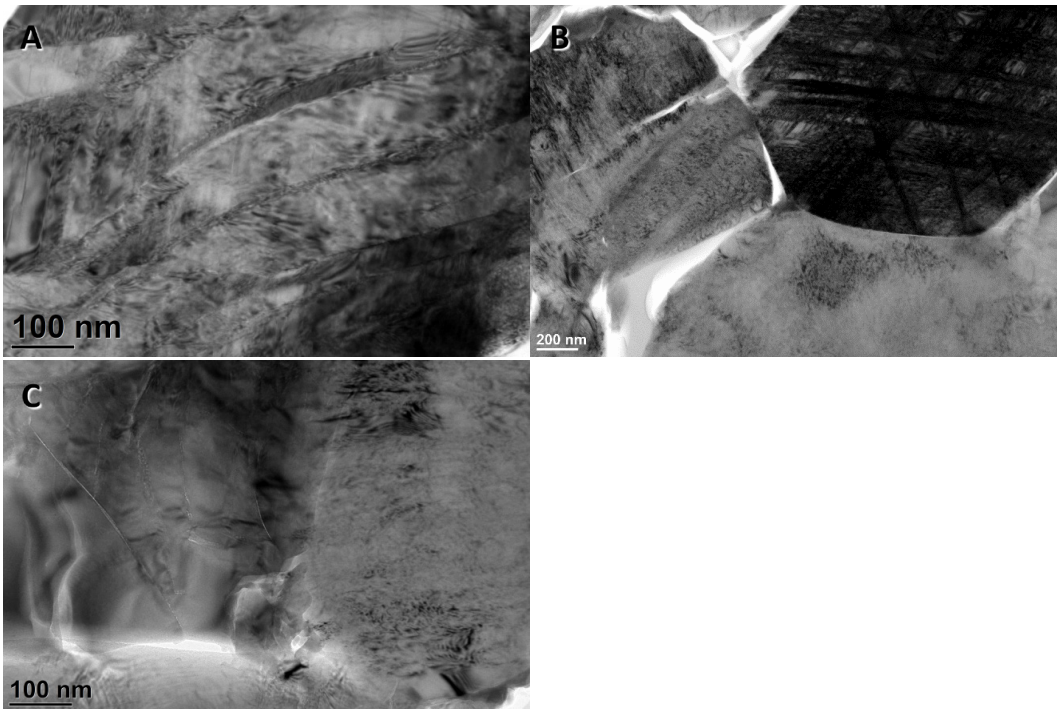

Fig. 25 A), B), and C) TEM-BF images showing high strain contrast due to high defect densities within grains under the indent in SiC-ESK

4. Conclusions

Initial examination of the three commercial SiCs showed that SiC-ESK had the smallest grain size, averaging 0.5–1 μm, while SiC-N and SiC-Hexoloy were of approximately equal size, averaging 5–10 μm. Each of the material's inherent crystalline defects consisted of mostly stacking faults with a few dislocations. SiC-ESK and SiC-Hexoloy exhibited the lowest densities of defects while SiC-N exhibited the highest.

After examination of the three SiCs after indentation, we found that heavy defect structures, including stacking faults and dislocations, were generated below the inelastic zones of all of the materials. TEM-BF imaging of the samples showed the presence of extremely high strain due to the high defect densities. Each material also exhibited both intergranular and intragranular cracking. With its intergranular phase inherent by design, the SiC-ESK was observed to have the most intergranular cracking followed by SiC-N and then SiC-Hexoloy, which had the least. By contrast, the SiC-Hexoloy exhibited the most intragranular cracking because of its larger grain size and clean grain boundaries. SiC-ESK, with its smaller grain size, which leads to more triple points, also exhibited a high degree of intragranular cracking. SiC-N, with its higher density of dislocations and stacking faults, exhibited the least amount of intragranular cracking due to the defects allowing

more plastic deformation to occur. Although not explicitly pointed out earlier, intergranular oxide phases are also subject to intragranular cracking and can be seen in some of the micrographs.

Also of note, triple junctions are stress concentration sites and can cause not only intragranular cracking, but also nucleation of dislocations. Additionally, deformation within grains under the indent was mainly due to dislocations and stacking faults as opposed to cracking. And finally, the presence of intergranular oxide films and phases changes the spatial extent of plastic deformation and intergranular cracking under the indent.

5. References

1. Beylat L, Cottenot CE. Post-mortem microstructural characterization of SiC materials after interaction with a kinetic energy projectile. WIT Transactions on the Built Environment: Structures under Shock and Impact IV. 1996;22:458–468.

2. Ray D, Flinders RM, Anderson A, Cutler RA, Campbell J, Adams JW. Effect of microstructure and mechanical properties on the ballistic performance of SiC-based ceramics. In: Franks LP, editor. Ceramic Engineering and Science Proceedings: Advances in Ceramic Armor II. Hoboken (NJ): John Wiley & Sons; 2007. p. 85–96.

3. Karandikar PG, Evans G, Wong S, Aghajanian MK, Sennett M. A review of ceramics for armor applications. In: Franks LP, editor. Advances in Ceramic Armor IV. Hoboken (NJ): John Wiley & Sons; 2009. p. 163–178.

4. Ray D, Flinders RM, Anderson A, Cutler RA, Rafaniello W. Effect of room-temperature hardness and toughness on the ballistic performance of SiC-based ceramics. In: Swab JJ, editor. Advances in Ceramic Armor. The American Ceramic Society; 2005. p. 131–142.

5. Matchen B. Applications of ceramics in armor products. Advanced Ceramic Materials: Applications of Advanced Materials in a High-Tech Society I. 1996;122-1:333–342.

6. Wereszczak AA, Johanns KE. Spherical indentation of SiC. In: Franks LP, editor. Advances in Ceramic Armor II. Hoboken (NJ): John Wiley & Sons; 2006. Vol. 27. p. 43–57.

7. Flinders M, Ray D, Cutler RA. Toughness-hardness trade-off in advanced SiC armor. In: Medvedovsk E, editor. Ceramic armor and armor systems. Hoboken (NJ): John Wiley & Sons; 2003;151:37–48.

8. Medvedovsk E. Silicon carbide-based ceramics for ballistic protection. In: Ceramic Armor and Armor Systems. Medvedovsk E, editor. Hoboken (NJ): John Wiley & Sons; 2003;151:19–25.

9. Flinders M, Ray D, Anderson A, Cutler RA. High-toughness silicon carbide as armor. J Am Cer Soc. 2005;88(8):2217–2226.

10. LaSalvia JC, Normandia MJ, Miller HT, Mackenzie DE. Sphere impact induced damage in ceramics: I. Armor-grade SiC and TiB_2. In: Swab JJ, editor. Advances in Ceramic Armor. The American Ceramic Society; 2005. V26, N7.

11. Medvedovski E. Advanced ceramics for personnel armor: current status and future. In: Ceramic Armor and Armor Systems II. Medvedovsk E, editor. The American Ceramic Society; 2006;178:3–18.

12. Luo H, Chen WW, Rajendran AM. Dynamic compressive response of damaged and interlocked SiC-N ceramics. J Am Cer Soc. 2006;89(1):266–273.

13. Lankford J, Predebon WW, Staehler JM, Subhash G, Pletka BJ, Anderson CE. The role of plasticity as a limiting factor in the compressive failure of high strength ceramics. Mechanics of Materials. 1998;29:205–218.

14. Danzer R, Lube T, Morrell R, Supancic P. Mechanical properties of ceramics. Handbook of advanced ceramics. 2nd ed. Chap 9.1, 2013.

15. Chen MW, McCauley JW, Dandekar DP, Bourne NK. Dynamic plasticity and failure of high-purity alumina under shock loading. Nature Materials. 2006;5:614–618.

16. Paliwal B, Ramesh KT, McCauley JW, Chen M. Dynamic compressive failure of AlON under controlled planar confinement. J Am Cer Soc. 2008;91(11):3619–3629.

17. Wilkins ML, Cline CF, Honodel CA. Fourth progress report of light armor program. Cal. Livermore: Lawrence Radiation Laboratory Univ; 1969 June 4.

18. Heard HC, Cline CF. Mechanical-behavior of polycrystalline BeO, Al_2O_3 and AlN at high-pressure. J Mat Sci. 1980;15(8):1889–1897.

19. Lundberg P, Renstrom R, Lundberg B. Impact of metallic projectiles on ceramic targets: transition between interface defeat and penetration. Int J Impact Eng. 2000;24(3):259–275.

20. Horii H, Nemat-Nasser S. Brittle failure in compression: splitting, faulting and brittle-ductile transition. Phil Trans Roy Soc A. 1986;319(1549):337–374.

21. LaSalvia JC, Campbell J, Swab JJ, McCauley JW. Beyond hardness: ceramics and ceramic-based composites for protection. J Minerals, Metals & Materials Soc. 2010;62(1):16–23.

22. Wilantewicz TE, McCauley JW. Analysis of hardness indentation size effect (ISE) curves in ceramics: a new approach to determine plasticity. 32nd Int Conf Adv Ceram. 2008.

23. Hilton CD, McCauley JW, Swab JJ, Shanholtz ER, Chen MW. Using hardness tests to quantify bulk plasticity and predict transition velocities in SiC materials. Int J Appl Ceram Technol. 2013;10(1):114–122.

24. Weiss Brennan CV, Walck SD, Swab JJ. A multi-step transmission electron microscopy sample preparation technique for cracked, heavily damaged, brittle materials. Microscopy and Microanalysis. 2014;20(6):1646–1653.

25. Lucas G, Burdet P, Cantoni M, Hebert C. Multivariate statistical analysis as a tool for the segmentation of 3D spectral data. Micron. 2013;52-53:49–56.

26. Kotula PG, Keenan MR, Michael JR. Automated analysis of SEM X-ray spectral images: a powerful new microanalysis tool. Microscopy and Microanalysis. 2003;9:1–17.

27. Keenan MR, Kotula PG. Accounting for Poisson noise in the multivariate analysis of ToF-SIMS spectrum images. Surface and Interface Analysis. 2004;36(3):203–212.

28. Maruyama T, Kitamura H, Iseki T. Microstructure and properties of sintered silicon carbides fabricated by different methods. Yogyo-Kyokai-Shi. 1986;94:(8):790–794.

29. Stevens R. Defects in silicon carbide. J Mat Sci. 1972;7(5):517–521.

30. Cantwell PR, Tang M, Dillon SJ, Luo J, Rohrer GS, Harmer MP. Grain boundary complexions. Acta Materialia. 2014;62:1–48.

31. Pabit E, Crane S, Seiban K, Butt DP, Ray D, Finders RM, Cutler RA. Grain boundary and triple junction chemistry of silicon carbide with aluminum or aluminum nitride additive. In: Medvedovsk E, editor. Ceramic Armor and Armor Systems II. The American Ceramic Society; 2006;178:91–102.

32. Swab JJ, Weiss Brennan CV, Walck SD, LaSalvia JC, Behler KD. An improved TEM sample preparation technique for heavily deformed ceramic materials having extensive sub-surface cracking. Microscopy and Microanalysis. 2005;21(S3):315–6.

List of Symbols, Abbreviations, and Acronyms

Al	aluminum
AlN	aluminum nitride
AlON	aluminum oxynitride
Al_2O_3	aluminum oxide
Ar	argon
BeO	beryllium oxide
BF	bright field
Cr	chromium
DF	dark field
Fe	iron
FIB	focused-ion beam
G.B.	grain boundary
HAADF	high-angle annular dark field
kg	kilograms
kgf	kilogram-force
MIMS	masked-ion milling system
mm	millimeters
μm	microns
MSA	multivariate statistical analysis
N	newton
nm	nanometer
rpm	revolutions per minute
s	second
SEM	scanning electron microscopy (or microscope)
σ_Y	compressive yield strength

Si	silicon
SiC	silicon carbide
STEM	scanning transmission electron microscopy (or microscope)
TEM	transmission electron microscopy (or microscope)
Ti	titanium
TiB_2	titanium diboride
V	vanadium
WC	tungsten carbide
XEDS	energy-dispersive X-ray spectroscopy
YAG	yttrium aluminum garnet
Zr	zirconium

1 (PDF) DEFENSE TECHNICAL INFORMATION CTR DTIC OCA

2 (PDF) DIR ARL
IMAL HRA
RECORDS MGMT
RDRL DCL
TECH LIB

1 (PDF) GOVT PRINTG OFC
A MALHOTRA

8 (PDF) ARL
RDRL WM
J ZABINSKI
RDRL WMM
M VANLANDINGHAM
RDRL WMM C
J SNYDER
S WALCK
RDRL WMM E
S HIRSCH
J LASALVIA
S SILTON
J SWAB